Comparative analysis of the thermoelectric properties of the non-textured and textured $Bi_{1.9}Gd_{0.1}Te_3$ compounds

Oleg Ivanov [a,b,*], Maxim Yaprintsev [a], Alexei Vasil'ev [a]

[a] *Belgorod State University, Belgorod, 394015, Russian Federation*
[b] *Belgorod State Technological University Named After V.G. Shukhov, Belgorod, 308012, Russian Federation*

ARTICLE INFO

ABSTRACT

Features in thermoelectric properties of non-textured and textured $Bi_{1.9}Gd_{0.1}Te_3$ compounds are analysed. Cold isostatic pressing was applied to prepare non-textured samples, whereas textured samples were fabricated via spark plasma sintering. The same starting powder was used for both preparation methods. Texturing [001] axis coincided with direction of spark plasma sintering pressuring. Thermoelectric properties of non-textured sample are isotropic, that is due to random grains orientation. Strong anisotropy in electrical resistivity and thermal conductivity, measured in directions parallel and perpendicular to direction of spark plasma sintering pressuring was found for textured sample. Texturing is partially recovering anisotropy inherent to single-crystalline bismuth telluride via redistributing anisotropic contributions from crystal *a-b* plane and *c*-axis into thermoelectric properties. Electrical resistivity decreases and thermal conductivity increases for parallel measuring orientation as compared to these properties for perpendicular measuring orientation. Highest thermoelectric figure-of-merit (~0.75 at ~420 K) was observed for textured sample for perpendicular measuring orientation.

1. Introduction

Generally, the physical properties of grained materials are remarkably dependent on various parameters of grain structure including the shape and size grains, the grain size distribution, the texturing degree, the specific properties of grain boundaries, etc. [1–8]. Grain boundaries contribution into the physical properties of the grained material can sufficiently modify relevant properties of the same material, but which is single crystal. Therefore, the grain boundaries engineering can be considered as one of effective ways to govern the physical properties of the grained materials and develop out new materials with desired properties. Particularly, this way is often and fruitfully applied to improve thermoelectric efficiency of nano- and micrograined materials [9–15]. It is known [16] that the thermoelectric efficiency of material can be expressed as the thermoelectric figure-of-merit, $ZT = TS^2/\rho k$, where T is the absolute temperature, ρ is the specific electrical resistivity, S is the Seebeck coefficient (the thermo-power) and k is the total thermal conductivity. All the thermoelectric properties (ρ, S and k) can be sensitive to presence and properties of the grain boundaries. The grain boundaries can act as scattering centers for electrons and phonons, affecting on ρ and k [17–20]. The grain boundaries can also enhance S via the electron energy filtering scenario [21–23]. In the grained thermoelectrics based on bismuth telluride, Bi_2Te_3, the grain boundaries are usually acting as *n*-type dopants, enhancing electron concentration [24–26]. Moreover, some thermoelectrics having a layered crystal structure, like Bi_2Te_3 and Bi_2Te_3-based alloys [27–38], SnSe [39–41], BiCuSeO [42], $Ca_3Co_4O_9$ [43,44], are readily textured via technological processes based on uniaxial pressuring a starting powder. For the textured samples, a preferential orientation of the grains takes place. The texturing allows partial recovering anisotropy in the thermoelectric properties of the grained material, which is inherent to single crystal. In this case, the properties, measured along directions parallel or perpendicular to the texturing axis, are rather different, that allows using the texturing to maximize ZT in the thermoelectric materials. The grain structure is dominantly controlled by the shape and size of particles in the starting powder, and by the conditions of compacting and sintering the starting powder, used to prepare bulk grained material. These conditions are dependent on way, chosen to compact and sinter the starting powder. At present, Bi_2Te_3 is one of end members, used to fabricate two-component thermoelectric *n*-type ($Bi_2Te_{3-x}Se_x$) and *p*-type ($Bi_{2-x}Sb_xTe_3$) solid solutions. The thermoelectric properties of these grained materials are strongly dependent on features in the grain structure, which can be tuned via changing parameters of preparation way.

The aim of this paper is to give a comparative analysis of relationship

---

* Corresponding author. Belgorod State University, Belgorod, 394015, Russian Federation.
E-mail address: Ivanov.Oleg@bsu.edu.ru (O. Ivanov).

between features in the grain structure and the thermoelectric properties of the *n*-type $Bi_{1.9}Gd_{0.1}Te_3$ compounds, prepared by two different ways using the same starting powder. The first way involves cold isostatic pressing (CIP), used to compact the started powder before its sintering [45]. The second way is spark plasma sintering (SPS), in which the compacting and sintering stages are simultaneously occurring [33]. The compounds studied were doped with Gd. It is known [33] that Gd, similarly to other rare earth elements (Lu, Ce, Sm, Er, La, etc. [46–56]), can be successfully used as donor dopant to remarkably enhance the thermoelectric figure-of-merit of Bi_2Te_3.

2. Materials and methods

Technological scheme, applied to prepare the bulk non-textured and textured $Bi_{1.9}Gd_{0.1}Te_3$ compounds with different grain structures, is presented in Fig. 1.

To prepare the $Bi_{1.9}Gd_{0.1}Te_3$ powder, the microwave-solvothermal synthesis was used. Details of the synthesis are given at top panel in Fig. 1. It is important to note that the synthesis applied allows preparing the powder, consisting of 2D-nanoplates. The as-synthesized powder was next used to prepare the bulk grained samples of two types, depending on preparing way. Compacting the as-synthesized powder and following sintering the compacted material were applied as separate technological stages for the first type samples (the CIP-samples), whereas for the second type samples (the SPS-samples) the compacting and sintering stages were be combined in a single process. Details of preparing the bulk samples are presented at bottom panels in Fig. 1 (left panel is for the CIP-sample, and right panel is for the SPS-sample). To study the thermoelectric properties, the $2 \times 2 \times 10$ mm bars and the $\text{Ø}10 \times 2$ mm disks were prepared.

Transmission electron microscopy (TEM) using a model JEM - 2100 microscope was applied to characterize the as-synthesized powder. X-ray diffraction (XRD) analysis was performed by using a Rigaku Ultima IV diffractometer with CuK_α – radiation to identify crystal structure and phase composition of the as-synthesized powder and the bulk materials. Density of the bulk samples was measured by the Archimedes method. A Shimadzu ICP (Inductively Coupled Plasma) emission spectrometer ICPE-9000 was applied to determine correct elemental composition of the bulk samples. Scanning electron microscopy (SEM) using a Nova NanoSEM 450 microscope was involved to study the grain structure features of the bulk samples. The specific electrical resistivity and the
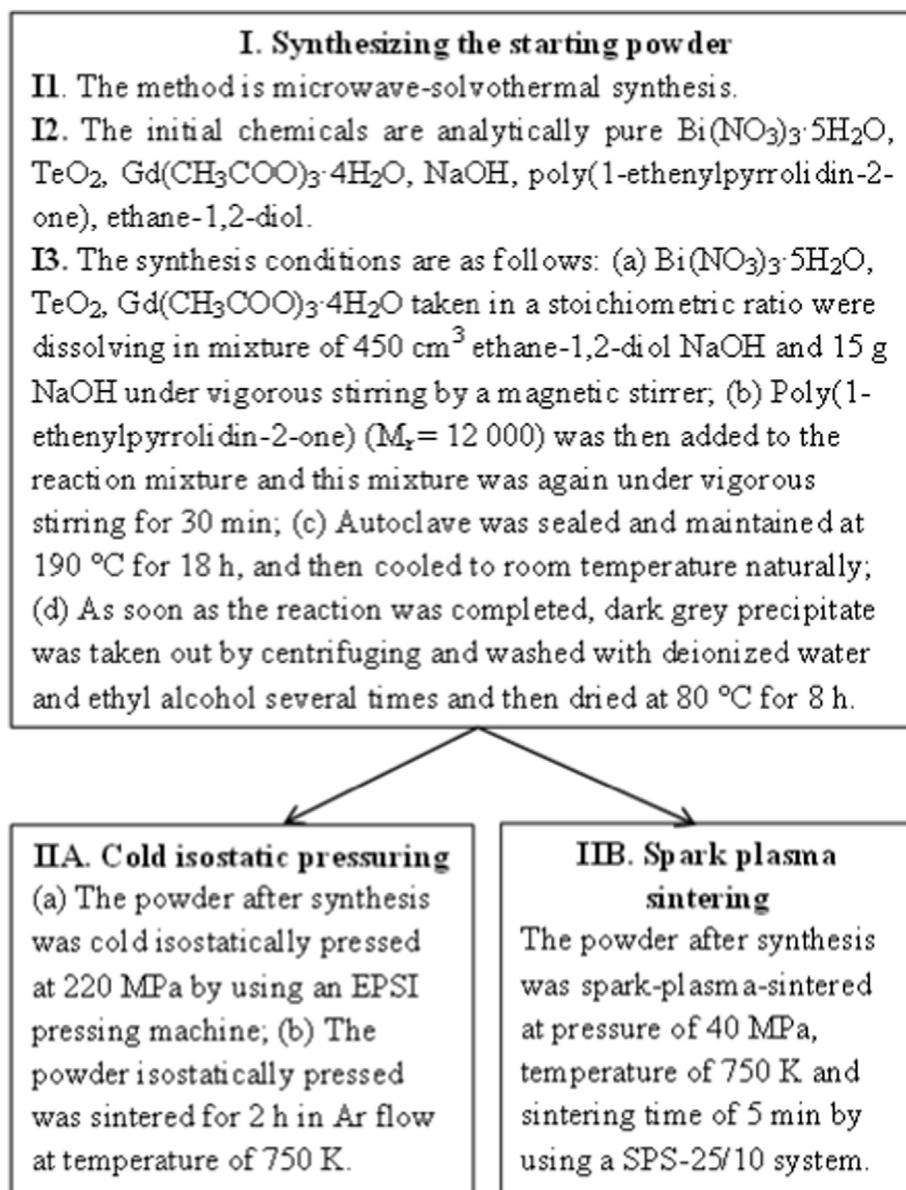

I. Synthesizing the starting powder

I1. The method is microwave-solvothermal synthesis.

I2. The initial chemicals are analytically pure $Bi(NO_3)_3 \cdot 5H_2O$, TeO_2, $Gd(CH_3COO)_3 \cdot 4H_2O$, NaOH, poly(1-ethenylpyrrolidin-2-one), ethane-1,2-diol.

I3. The synthesis conditions are as follows: (a) $Bi(NO_3)_3 \cdot 5H_2O$, TeO_2, $Gd(CH_3COO)_3 \cdot 4H_2O$ taken in a stoichiometric ratio were dissolving in mixture of 450 cm^3 ethane-1,2-diol NaOH and 15 g NaOH under vigorous stirring by a magnetic stirrer; (b) Poly(1-ethenylpyrrolidin-2-one) ($M_r = 12\,000$) was then added to the reaction mixture and this mixture was again under vigorous stirring for 30 min; (c) Autoclave was sealed and maintained at 190 °C for 18 h, and then cooled to room temperature naturally; (d) As soon as the reaction was completed, dark grey precipitate was taken out by centrifuging and washed with deionized water and ethyl alcohol several times and then dried at 80 °C for 8 h.

IIA. Cold isostatic pressuring

(a) The powder after synthesis was cold isostatically pressed at 220 MPa by using an EPSI pressing machine; (b) The powder isostatically pressed was sintered for 2 h in Ar flow at temperature of 750 K.

IIB. Spark plasma sintering

The powder after synthesis was spark-plasma-sintered at pressure of 40 MPa, temperature of 750 K and sintering time of 5 min by using a SPS-25/10 system.

Fig. 1. Technological scheme of preparing the bulk non-textured and textured $Bi_{1.9}Gd_{0.1}Te_3$ compounds.

Seebeck coefficient of the bar samples were measured by using a ZEM-3 system. The total thermal conductivity of the disk-shaped samples was measured by a TC-1200 system using a laser flash method. The concentration, n, and Hall mobility, μ_H, of electrons were estimated from studying the Hall effect by using a Mini Cryogen Free Measurements System (Cryogenic Ltd, UK).

3. Results and discussion

3.1. Texturing in the Bi_2Te_3-based compounds

The crystal Bi_2Te_3 structure is known to be layered one [57,58]. Crystal c-axes are perpendicular to the layers, and neighboring layers are bonded via weak Van-der-Waals interaction, whereas crystal $a - b$ planes are oriented along the layers, and the chemical bonding between atoms within the layers is dominantly strong covalent. Owing to different nature of the chemical bonding existing between and along the layers, a growth of the Bi_2Te_3 particles during chemical synthesis happens is 2D-growth, since growth rates for directions, parallel and perpendicular to the layers, are rather different. Shape, size and dimensionality of the particles in the as-synthesized powder are the parameters, strongly affecting on the grain structure of the bulk material, prepared from this powder. The 2D (plates) or 1D (whiskers) particles are usually forming the shape-anisotropic grains with big grain shape factor in relevant bulk materials. Particularly, in these materials the shape-anisotropic grains can be preferentially ordered in some plane that results in developing a texturing. Will the texturing really take place or not, is dependent on a pressuring way, acting during compacting the starting powder or sintering the preliminary compacted material. Under isostatic pressuring, the powder being compacted is subjected to equal pressure from all directions, i.e. molded body is compressed uniformly over its entire surface. The material compacted by isostatic pressuring will be characterizing by random orientation of the grains, similarly to chaotic arrangement of the plate-like or whisker-like particles in the starting powder, although themselves grains can remain to be highly shape-anisotropic. The isostatic pressuring is applied at the cold and hot isostatic pressuring methods. In contrast to the isostatic pressuring methods, at spark plasma sintering, as at common method of die pressuring, uniaxial pressuring is applied to one surface of molded body, that

results in its compression along direction, perpendicular to this surface. To release the strain, created by uniaxial pressuring, the shape-anisotropic grains, being formed from the plate-like or whisker-like particles of the starting powder, will be preferentially arranged in the plane oriented perpendicularly to pressing direction, resulting in the texturing. Two special directions should be introduced for the textured samples to characterize the texturing. One of them is texturing axis usually coinciding with applied uniaxial pressuring, i.e. this direction is perpendicular to plane with preferential arrangement of the grains, whereas the second direction is positioned in this plane.The grained structures of these samples are schematically shown in bottom part of Fig. 2. Each individual grain assumed to be parallelepiped-shaped. Hence, the grain is imaged as a rectangular in plane. Rectangular shape can clearly underline anisotropy in the thermoelectric properties, inherent for the individual Bi_2Te_3 grain. If long side of the rectangular is parallel to the crystal layers mentioned above, then the thermoelectric properties, measured along this side, are determined by the properties, characteristic for crystal $a - b$ planes (ρ_{ab}, k_{ab} and S_{ab}), whereas the thermoelectric properties, taken perpendicularly to this side, are characteristic for crystal c-axes (ρ_c, k_c and S_c). Since the grained structure of the non-textured sample is disordered and characterized by random orientation of the grains, the thermoelectric properties of this sample is isotropic, i.e. the properties are the same (ρ_i, k_i and S_i) for any measuring direction. To underline this isotropy, shape of the non-textured-sample is chosen as a ball (or a circle for the plane image in Fig. 2). In turn, the grains in the SPS-sample preferentially lie in the planes, perpendicular to the SPS-pressing direction. In this sample crystal c-axes of the grains are preferentially directed parallel to the SPS-pressing direction, while crystal a-b planes of the grains are preferentially oriented perpendicularly to this direction. Hence, anisotropy in the thermoelectric properties, inherent to individual single-crystalline grain, can be partially recovered under the texturing, i.e. the properties, measured along directions perpendicular or parallel to the SPS-pressing direction in the grained material, will be different. The ρ_{ab}, k_{ab} and S_{ab} values will dominantly contribute into the relevant thermoelectric properties, measured in the perpendicular direction, $\rho\perp$, $k\perp$ and $S\perp$, whereas the thermoelectric properties in the parallel direction, $\rho_\parallel$, $k_\parallel$ and $S_\parallel$, will be preferentially governed by the ρ_c, k_c and S_c contributions, respectively. To underline anisotropy in the thermoelectric properties, shape of the textured sample
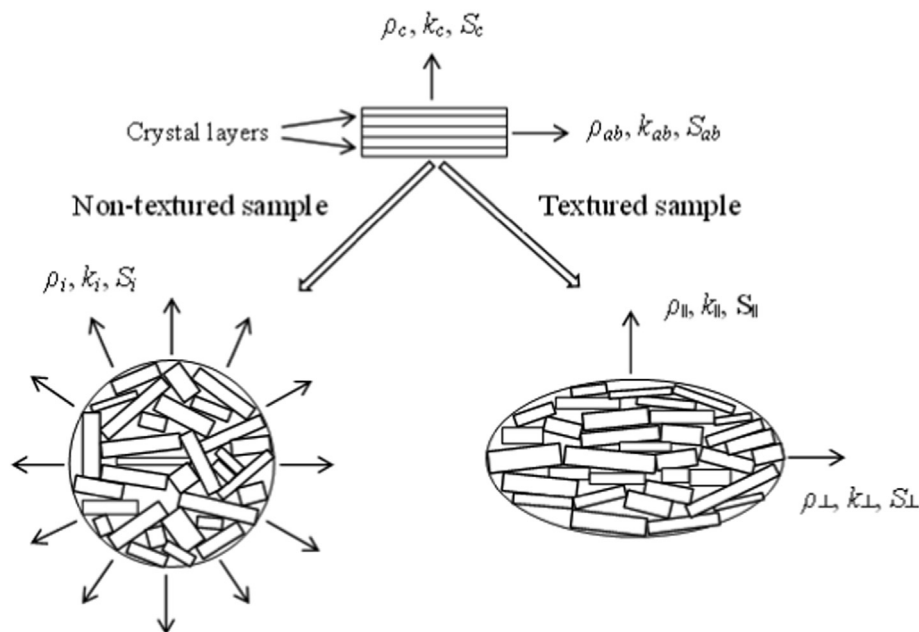

Fig. 2. Schematic images of the grain structures for the non-textured sample (bottom-left image) and the textured sample (bottom-right image). Top image is an individual grain.

is chosen as an ellipsoid (or an ellipse for the plane image in Fig. 2). In this case, two semi-axes of the ellipse can be related to anisotropy in the properties, measured along these semi-axes.

For Bi_2Te_3, anisotropy in the thermoelectric properties is described as $\rho_c/\rho_{ab} \approx 5 \div 5.5$ for the electrical properties, and $k_{ab}/k_c \approx 2$ for the total thermal conductivity [34,35,59]. However, in contrast to k and ρ, the Seebeck coefficient is far less anisotropic quantity. To characterize the difference between the isotropic thermoelectric properties of the CIP-sample and the anisotropic thermoelectric properties of the SPS-sample, it would be helpful to introduce the following tensors

$$T_{CIP} = \begin{vmatrix} T_i & 0 & 0 \\ 0 & T_i & 0 \\ 0 & 0 & T_i \end{vmatrix} \tag{1a}$$

for the CIP-sample, and

$$T_{SPS} = \begin{vmatrix} T_\perp & 0 & 0 \\ 0 & T_\perp & 0 \\ 0 & 0 & T_\parallel \end{vmatrix} \tag{1b}$$

for the SPS-sample, where $T = \rho$, k and S.

The (1a) tensor is corresponding to the isotropic thermoelectric properties of the non-textured sample, whereas the thermoelectric properties of the textured sample, differing for two measuring directions, are presented in the (1b) tensor. This difference will be dependent on initial anisotropy in the thermoelectric properties, inherent to single-crystalline material, used to prepare relevant grained material, and on a texturing degree, characterizing a degree of preferential grain orientation.

3.2. Texturing in the XRD- and SEM-examination of the $Bi_{1.9}Gd_{0.1}Te_3$ compounds

According to XRD analysis (Fig. 3 (a), left panel), the as-synthesized powder is single hexagonal $R\overline{3}m$ phase, which is corresponding to pure Bi_2Te_3 (PDF#01-089-4302). By using TEM examination, the as-synthesized powder is mainly consisted of hexagonal plate-shaped particles with average plate size of a few hundreds of nm and width of ~100 nm (Fig. 3 (a), right panel). Therefore, separate particles in the as-synthesized powder can be really considered as hexagonal 2D-nanoplates. Hexagonal habitus, observed for the single-crystalline particles, is corresponding to hexagonal symmetry of itself compound studied. As was mentioned above, forming the 2D-nanoplates during a chemical synthesis is typical for compounds, based on Bi_2Te_3 and originated from specific features in crystal structure and chemical bonding of Bi_2Te_3. Elemental composition of the nanoplates was earlier examined by the EDX method [33]. According to this examination, Gd is in fact inserted in the nanoplates and all the elements (Bi, Te and Gd) are uniformly distributed within the plates. The as-synthesized powder was further applied to prepare the CIP- and SPS-samples.

Usually, two special directions in the textured samples are clearly confirmed by the XRD and SEM examination. The XRD patterns, as and the shape and size of the grains, extracted from the SEM images, corresponding to surfaces oriented parallel or perpendicularly to uniaxial pressuring direction, are rather different. The XRD pattern for the CIP-sample is mainly coinciding with the XRD pattern for the as-synthesized powder, i.e. both the positions of peaks and the ratio of their intensities do not change (Fig. 3 (b), left panel). Disordered grain structure with the grains having mainly plate-like shape is also observed for this sample (right panel).

For the SPS-sample, a look of the XRD pattern is dependent on orientation of the surface, used to take the XRD pattern, regarding to the SPS-pressuring direction. For the surface, perpendicular to this direction, the (11l) peaks are dominant, whereas all other peaks are strongly weakened (Fig. 3 (c), left panel). For the surface, parallel to the SPS-

pressuring direction, the (001) peaks are already dominant ((Fig. 3 (d), left panel). However, both XRD patterns are still matching to the $R\overline{3}m$ symmetry, i.e. the positions of the peaks observed are in total agreement with this crystal symmetry and only redistribution in the peaks intensity occurs. Such kind of redistribution can really occur, if crystal $a – b$ planes in the grains of the textured samples are preferentially oriented perpendicularly to the SPS-pressuring direction. In other words, the crystal layers governing anisotropy in the physical properties of the Bi_2Te_3-based compounds and mentioned above, are preferentially positioned in the planes, perpendicular to this direction. Similarly to the XRD patterns, the SEM images, recorded on the fractured surfaces, oriented perpendicularly and parallel to the SPS-pressing direction, are also different. Disordered grain structure with the irregular shaped-grains is observed at the perependicular surface, whereas the grains form ordered lamellar structure at the parallel surface. The lamellar sheets consist of the grains, elongated in plane perpendicular to the SPS-pressing direction, i.e. the sheets lie in plane, perpendicular to this direction. Thus, using the same as-synthesized powder, one can prepare either non-textured grained samples via cold isostatic pressuring or textured grained samples via spark plasma sintering.

To estimate the degree of preferential grain orientation in the textured material, the Lotgering factor, F, is usually applied [60]. The F value for the SPS-sample studied was extracted by analysis of the XRD patterns, presented in Fig. 3 (c) and (d), by using expressions

$$F = \frac{p - p_0}{1 - p_0}, \tag{2a}$$

with p and p_0 are defined as

$$p = \frac{I(00l)}{\sum I(hkl)}, \ and \ p_0 = \frac{I_0(00l)}{\sum I_0(hkl)}, \tag{2b}$$

where the I and I_0 intensities are corresponding to the textured and non-textured samples, respectively. In limiting cases, $F \to 1$ is for ideally textured (like single crystal) samples, and $F \to 0$ is for completely non-textured samples (powder or the grained material with completely random grain orientation).

The F value was estimated as ~0.68, that is characteristic for highly-textured material. All the parameters, characterizing the CIP- and SPS-samples, can be divided into isotropic (Table 1) and anisotropic (Table 2) parameters. These parameters were taken at room temperature. The isotropic parameters are the density, d, the elemental composition, and the electron concentration. The density of the SPS-sample is higher as compared to that for the CIP-sample. This difference in the density can be originated from features of ways, applied to compact and sinter these samples. Although maximum pressuring value is higher at the CIP-process, in this case compacting stage of the starting powder is preceding to following high-temperature sintering stage. At the SPS-process, stages of compacting and sintering are implemented simultaneously at high temperatures under simultaneous acting both uniaxial pressuring and pulse electrical current. Extra mechanisms of an interstitial diffusion can be involved in densification process for the SPS-sample, which are based on electrical diffusion and reducing the diffusion constant under the applied SPS-pressuring [61–67]. These mechanisms will result in higher densification of the SPS-sample as compared to that of the CIP-sample.

Slight difference in the elemental composition of the CIP- and SPS-samples was found, too. Changing in the elemental composition of the Bi_2Te_3-based compounds during the sintering is usually related to high-temperature evaporation of Te, which is due to remarkable difference in the energy evaporation of Te (52.55 $kJ·mol^{-1}$) and Bi (104.80 $kJ·mol^{-1}$) [48]. This evaporation resulted in deviation of real elemental composition of the CIP- and SPS-samples from nominal $Bi_{1.9}Gd_{0.1}Te_3$ composition. In contrast to Te, the Bi and Gd content was found to be practically T-independent, i.e. the changes of stoichiometric composition
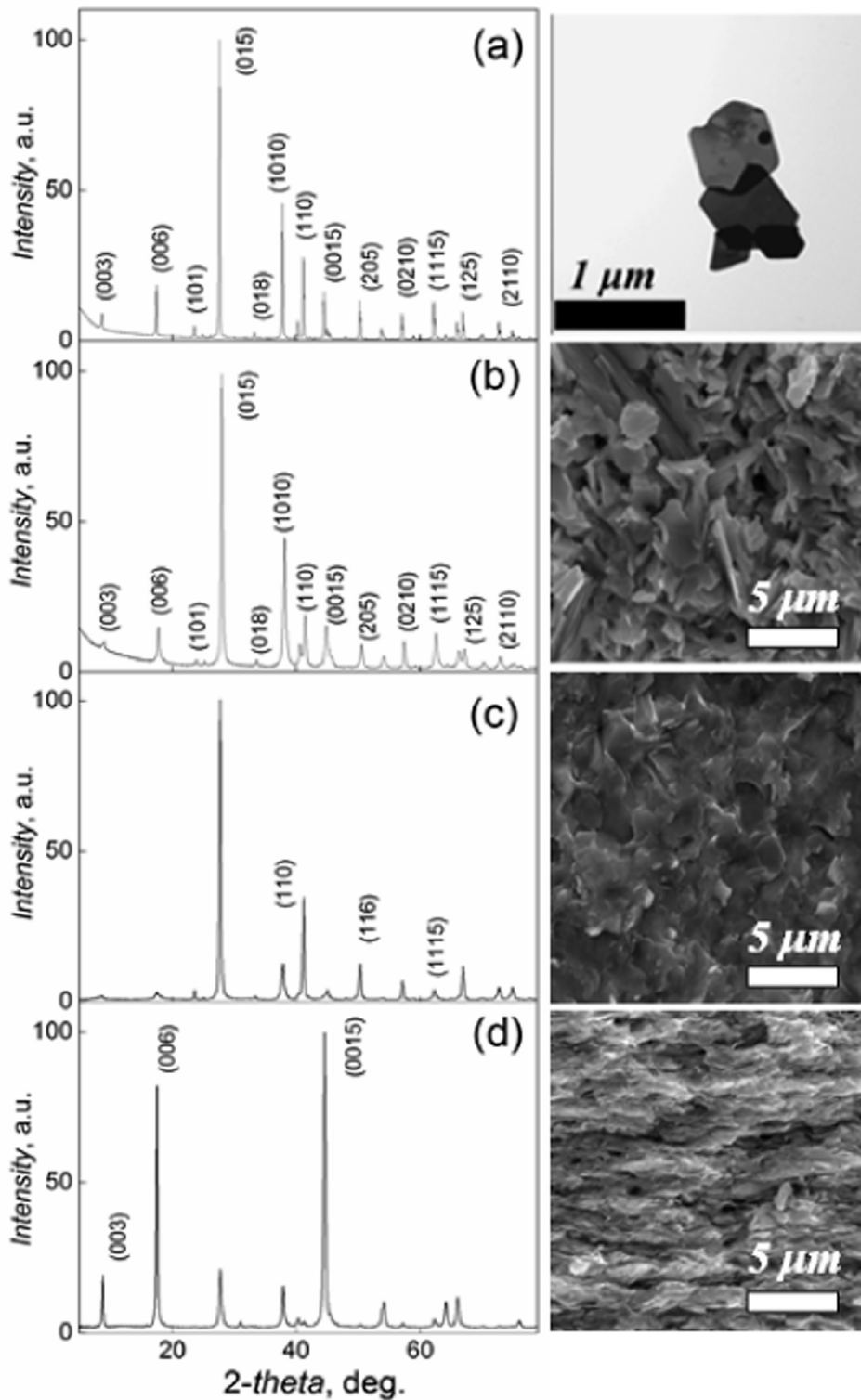
Fig. 3. (a) Left panel: the XRD pattern for the as-synthesized $Bi_{1.9}Gd_{0.1}Te_3$ powder; right panel: the TEM-image of the plate-like particles in the as-synthesized powder; (b) Left panel: the XRD pattern for the CIP-sample; right panel: the SEM image taken on the fractured surface of this sample; (c) Left panel: the XRD pattern for the SPS-sample taken on surface oriented perpendicularly to the SPS-pressing direction; right panel: the SEM image of this surface; (d) Left panel: the XRD pattern for the SPS-sample taken on the surface oriented parallel to the SPS-pressing direction; right panel: the SEM image of this surface.

observed in the samples should be attributed to the change in the Te content. The Te evaporation is more effective for the SPS-sample, although the sintering time for this sample is far less than the time of high-temperature annealing for the CIP-sample (5 min against 2 h). Real evaporation process is rather complicated and can involve a few diffusion mechanisms (volume diffusion, grain boundary diffusion and surface diffusion), which are usually related to vacancy gradient concentration. At the SPS-process, extra diffusion mechanisms can accelerate a total

diffusion process, resulting in intensive Te evaporation. The Te content in the SPS-sample happens is less as compared to that in the CIP-sample. Decreasing in the Te content is naturally resulting in formation of Te vacancies, $V_{Te}^{..}$, within the crystal Bi_2Te_3 structure. Each positively charged $V_{Te}^{..}$ vacancy will generate two free electrons, as follows from equation [25].
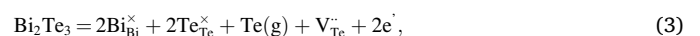
$$Bi_2Te_3 = 2Bi_{Bi}^{\times} + 2Te_{Te}^{\times} + Te(g) + V_{Te}^{..} + 2e^{'}, \qquad (3)$$

Table 1
Isotropic parameters of the CIP- and SPS-samples.

Sample	d, g/cm^3	Elemental composition	n, 10^{19}, cm^{-3}
CIP-sample	6.8	Bi$_{1.9}$Gd$_{0.1}$Te$_{2.956}$	4.3
SPS-sample	7.5	Bi$_{1.9}$Gd$_{0.1}$Te$_{2.897}$	4.9

Table 2
Anisotropic parameters of the CIP- and SPS-samples.

Sample	$D\perp$, nm	$D_{\parallel}$, nm	$\mu_H\perp$, cm$^2\cdot$V$^{-1}\cdot$s^{-1}	$\mu_{H\parallel}$, cm$^2\cdot$V$^{-1}\cdot$s^{-1}
CIP-sample	1175		145	
SPS-sample	865	145	225	40

where symbol g is corresponding to a gaseous phase.

In accordance with equation (3), the electron concentration should be increased with increasing in the $V_{Te}^{..}$ vacancy content. This behavior was really found for the CIP- and SPS-samples.

Anisotropic parameters are the average grain size, D, and the electron mobility, μ_H. These parameters are dependent on measuring direction in the SPS-sample, i.e. the $D\perp$ and $D_{\parallel}$, and $\mu_H\perp$ and $\mu_{H\parallel}$ values should be used in this case. Here the $\perp$ and $\parallel$ subscripts correspond to the directions, perpendicular or parallel to the SPS-pressuring direction, respectively. For the CIP-sample, the $D\perp = D_{\parallel}$ and $\mu_H\perp = \mu_{H\parallel}$ equalities are naturally valid. To estimate the average grain size in the CIP- and SPS-samples, the histograms of the grain size distribution were plotted using the SEM images in Fig. 3. Next, these histograms were analysed by lognormal unimodal distribution fittings [68]. For the CIP-sample, the average grain size is remarkably bigger than the $D\perp$ and $D_{\parallel}$ values, estimated for the SPS-sample. Generally, high-temperature growth of the grains in the grained samples results in reducing in energy of system with numerous interfaces. According to Ref. [69,70], general equation, used to describe the grain growth, can be expressed as

$$D_t^m - D_0^m = Ct\exp\left(-\frac{E_a}{RT}\right), \qquad (4)$$

where D_t and D_0 are the average grain size at time t and the original grain size, respectively, m is the grain growth exponent, t is the sintering time, E_a is the grain growth activation energy, C is the pre-exponential constant and R is the general gas constant.

In accordance with expression (4), bigger size of the grains for the CIP-sample can be attributed to longer sintering time. It should be also noted that for the SPS-sample $D\perp$ is much bigger than $D_{\parallel}$. The big difference in $D\perp$ and $D_{\parallel}$ is characteristic for highly shape-anisotropic grains. As was mentioned above, the bulk sample having such grains is readily textured under uniaxial pressuring. A grain shape factor, $D\perp/D_{\parallel}$, was found to be equal to ~6.

The electron mobility for the CIP-sample is intermediate between the $\mu_H\perp$ and $\mu_{H\parallel}$ values for the SPS-sample. Difference in $\mu_H\perp$ and $\mu_{H\parallel}$ is dominantly originated from partial recovering in anisotropy on the electron mobility, inherent to single crystal. This inherent anisotropy is responsible for the $\rho_c/\rho_{ab} \approx 5 \div 5.5$ anisotropy in the thermoelectric properties (It is known [71] that the specific electrical resistance of n-type semiconductors is expressed as $\rho = 1/(en\mu)$, where e is the electron charge). Besides, the grain boundary scattering can be also considered as one more mechanism, affecting on anisotropy in $\mu_H\perp$ and $\mu_{H\parallel}$. Since the average grain size for the direction perpendicular to the SPS-pressing direction is much bigger than for the parallel direction, more number of the grain boundaries, acting as the scattering centers for electrons, exist for the parallel direction. So, for this orientation the grain boundary scattering should be more effective, resulting in additional reducing in $\mu_{H\parallel}$ as compared to $\mu_H\perp$. Anisotropy in the electron mobility is characterized as $\mu_H\perp/\mu_{H\parallel} \approx 5.6$.

3.3. Texturing effect on the thermoelectric properties of the Bi$_{1.9}$Gd$_{0.1}$Te$_3$ compounds

The thermoelectric properties of the CIP- and SPS-samples were examined within the 285–615 K range. For the SPS-sample, the thermoelectric properties were measured for the perpendicular and parallel measuring directions. The temperature dependences of the specific electrical resistivity, the Seebeck coefficient and the power factor, PF,

calculated as S^2/ρ, are presented in Fig. 4. The electrical resistivities of all the samples (ρ_i, $\rho\perp$, $\rho_{\parallel}$) are gradually increasing with increasing temperature within whole temperature range. As was concluded earlier [37,45], such temperature behavior of the electrical resistivity of Bi$_{1.9}$Gd$_{0.1}$Te$_3$ is really related to two mechanisms of the electrical conductivity, which succeed each other at gradual heating. The temperature, corresponding to changing in the conductivity mechanism, can be easily extracted by analyzing the $d\rho/dT$ vs. T curves, plotted in inset to Fig. 4 (a). Clear kinks can be found in these curves at some temperature T_d. Below T_d, the $\rho(T)$ behavior should be attributed to a regime of the degenerate semiconductor. The degenerate donor semiconductor is characterized by the T-independent electron concentration. The $\rho(T)$ behavior is mainly governed by the $\mu(T)$ behavior. For the temperatures considered, the optical and acoustic phonon scattering is dominant mechanism, responsible for the temperature μ change. At $T > T_d$, an onset of intrinsic conductivity due to a thermal excitation of the carriers from valence band to conduction band takes place. Both electrons in conduction band and holes in valence band are thermally generated, that results in decreasing in ρ via relevant increasing in current carrier concentration. The T_d temperature is different for the CIP-sample ($T_d \approx 500$ K) and the SPS-sample ($T_d \approx 450$ K). However, this T_d difference will not be discussed here. The $\rho_i(T)$ curve for the CIP-sample is positioned between the $\rho_{\parallel}(T)$ and $\rho\perp(T)$ curves, taken for the SPS-sample, and the $\rho_{\parallel}(T)$ curve lies higher $\rho\perp(T)$ curve. This behavior is expected and natural, since $\rho_{\parallel}$ is dominantly governed by the ρ_c resistivity, whereas the ρ_{ab} resistivity is dominantly contributing into $\rho\perp$, and $\rho_c > \rho_{ab}$. Therefore, the texturing is just redistributing the ρ_c and ρ_{ab} contributions into the total resistivity, that results in partial recovering in anisotropy in ρ.

In contrast to the $\rho(T)$ behavior, difference in the $S(T)$ behavior for the CIP- and SPS-samples is far less expressed (Fig. 4 (b). Sign of S is negative in agreement with the n-type conductivity of samples studied. The small difference in $S_i(T)$, $S_{\parallel}(T)$ and $S\perp(T)$ curves is expected, since the Seebeck coefficient is weakly anisotropic quantity. All the curves are bell-like shaped, that is typical for the doped Bi$_2$Te$_3$ and Bi$_2$Te$_3$-based compounds [46–48]. The maximum S value was observed for the SPS-sample at parallel measuring direction ($|S\perp| \approx 148$ µV/K at ~450 K), whereas minimum S value was found for the CIP-sample ($|S_i| \approx 135$ µV/K at ~500 K). It is important to note that the temperatures of the S_i, and $S\perp$ and $S_{\parallel}$ maxima coincide with the T_d temperatures, extracted from the $d\rho/dT$ vs. T curves for the same samples.

Fig. 5 (a) shows the temperature dependences of the total thermal conductivity for the CIP- and SPS-samples.

The $k_i(T)$, $k_{\parallel}(T)$ and $k\perp(T)$ curves qualitatively behave in the same manner. At heating, the thermal conductivity of all the samples is gradually decreasing, but above some temperature (~400 K for the CIP-sample and ~375 K for the SPS-sample) the thermal conductivity is steady increasing, i.e. minima in the $k_i(T)$, $k_{\parallel}(T)$ and $k\perp(T)$ curves takes place. Similarly to the features, observed in the $\rho(T)$ (the kinks in the $d\rho/dT$ vs. T curves, inset to Fig. 4) and S(T) (the maxima in Fig. 4 (b)) dependences, these k minima are also originated from changing in the mechanisms of the thermal conductivity. The lattice (or phonon) thermal conductivity, k_p, the electronic thermal conductivity, k_e, and the bipolar thermal conductivity, k_b, contribute to the $k(T)$ behavior, presented in Fig. 5 (a) [33,45]. For temperatures under consideration, k_e is practically T-independent. For temperatures below the k minima, the k behavior is dominantly attributed to changing in k_p [72]. According to the Dulong-Petit law, the phonon specific heat is constant for these temperatures. Phonon energy and number of phonons are linearly increasing with increasing temperature. Scattering rate of the phonons is
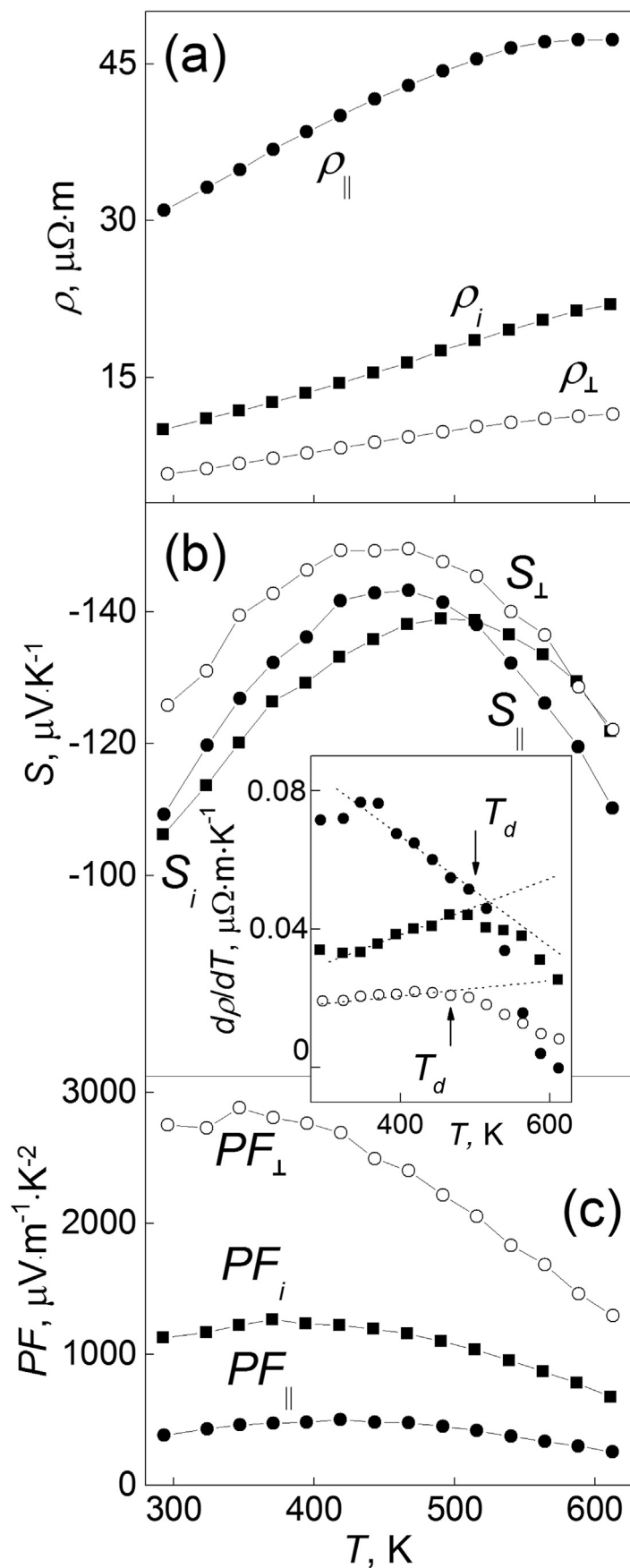
Fig. 4. The temperature dependences of the specific electrical resistivity (a), the Seebeck coefficient (b) and the power factor (c) for the CIP- and SPS-samples; inset shows the $d\rho/dT$ vs. T dependences.
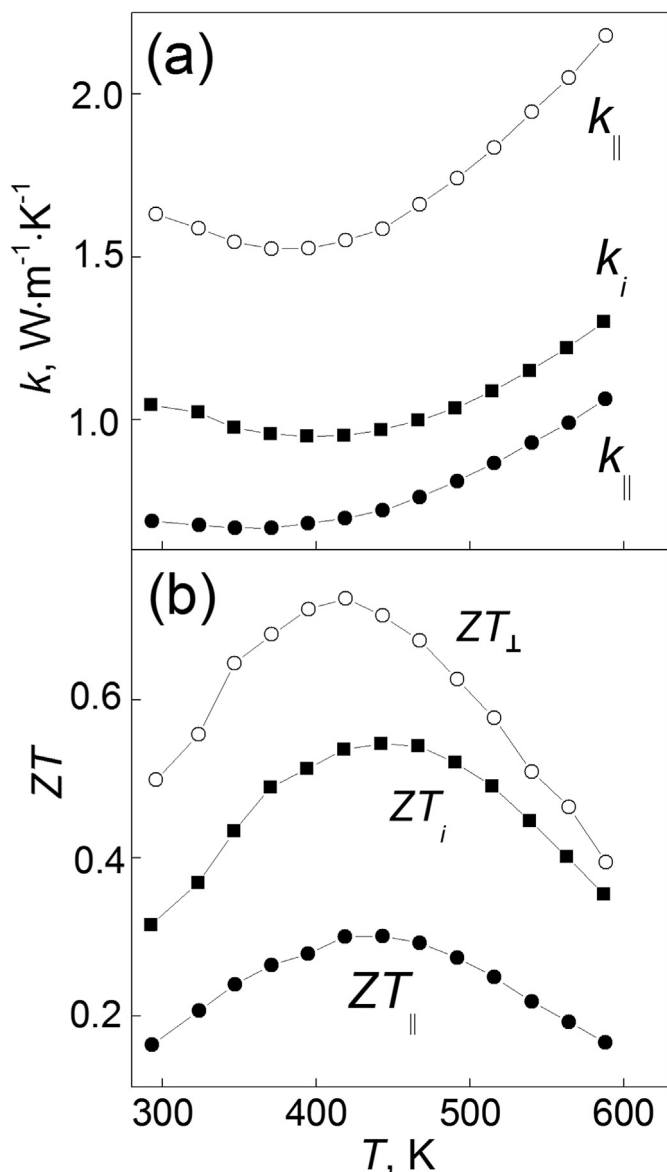
Fig. 5. The temperature dependences of the total thermal conductivity (a) and the thermoelectric figure-of-merit (b) for the CIP- and SPS-samples.

proportional to its number. Hence, k_p is also decreased with increasing temperature in agreement with the T^{-1} law. For temperatures above the k minima, the $k(T)$ behavior is dominantly governed by changing in k_b. At the bipolar thermal conductivity due to the intrinsic conductivity, the electron-hole pairs will be thermally excited at hot-side of sample and moved to cold-side [73]. Owing to lower temperature, a recombination of these neutral pairs will take place at cold-side. Energy of recombination per one electron-hole pair will be emerged as a phonon. The energy is equal or greater than the band gap. Results of detailed analysis of contributions from k_p, k_e and k_b into the $k_i(T)$, $k_\parallel(T)$ and $k\perp(T)$ curves for the CIP- and SPS-samples will be published elsewhere.

Similarly to the texturing effect on the electrical resistivity, k for the CIP- and SPS-samples is also changing under the texturing with clear and understandable manner. The $k_i(T)$ curve for the CIP-sample is positioned between the $k_\parallel(T)$ and $k\perp(T)$ curves, taken for the SPS-sample, and the $k\perp(T)$ curve lies higher $k_\parallel(T)$ curve. Due to partial recovering in inherent anisotropy, $k\perp$ for the perpendicular orientation is higher as compared to $k_\parallel$ for the parallel orientations. In this case, $k_\parallel$ is dominantly governed by the k_c thermal conductivity, whereas the k_{ab} thermal conductivity is dominantly contributing into $k\perp$, and $k_{ab} > k_c$.

Finally, the $\rho(T)$, $S(T)$ and $k(T)$ curves, taken for the CIP- and SPS-samples, were used to plot the $ZT(T)$ dependences (Fig. 5 (b)). All the $ZT(T)$ curves are bell-like shaped with maxima temperatures, falling in the 420–460 K interval. These maxima are resulted from the intrinsic conductivity, which is gradually developing at high temperatures and inducing the bipolar thermal conductivity. The bipolar thermal conductivity results in remarkable degrading in thermoelectric figure-of-merit. Owing the strong effect of the texturing on the specific electrical resistivity and the total thermal conductivity, the thermoelectric efficiency of the non-textured and textured $Bi_{1.9}Gd_{0.1}Te_3$ samples is remarkably different. As for the textured SPS-samples, the thermoelectric figure-of-merit for the perpendicular measuring orientation is much more as compared to that for the parallel measuring orientation. The $ZT_i(T)$ curve for the CIP-sample is positioned between the $\rho_\parallel(T)$ and $\rho\perp(T)$ curves, taken for the SPS-sample. For the perpendicular orientation, low ρ and high S, favouring to enhancing in ZT, but high k, harmful for final enhancing in ZT, are simultaneously observed. However, the ρ and S contributions are dominant, that results in enhancing in ZT. The highest ρ and lowest k values are observed for the SPS-sample for the parallel measuring orientation. However, the dominant ρ contribution prevents enhancing in $ZT_\parallel$, despite the low thermal conductivity for this measuring orientation. For the CIP-sample, the ρ and k values are intermediate between relevant values for the SPS-sample, taken for the perpendicular and parallel measuring orientations. For the perpendicular measuring orientation, the highest ZT value (~0.75) was observed at ~420 K.

4. Conclusion

Thus, comparative analysis of the microstructure (grain structutre) and thermoelectric properties of the no-textured and textured $Bi_{1.9}Gd_{0.1}Te_3$ compounds has been reported in detail. To correctly compare the isotropic and anisotropic thermoelectric properties, the non-textured and textured compounds were prepared from the same started powder. In this case, the non-textured sample can be correctly used as a reference sample. The texturing in the Bi_2Te_3-based materials is a physical phenomenon, important to control the thermoelectric properties. Different grain structure, characteristic for the non-textured and textured samples, was controlled via compacting way. Besides the texturing developing, different ways for preparing the samples can also affect on other parameters, which are important for the thermoelectric properties (density, elemental composition, grain size, mobility and concentration of electrons). The texturing is accompanied by the changing in these parameters.

Declaration of competing interest

The authors declare that they have no known competing financial interests or personal relationships that could have appeared to influence the work reported in this paper.

CRediT authorship contribution statement

Oleg Ivanov: Conceptualization, Writing - review & editing. **Maxim Yaprintsev:** Formal analysis, Writing - original draft. **Alexei Vasil'ev:** Investigation.

References

[1] D. Wolf, J. Lutsko, M. Kluge, Physical properties of grain-boundary materials: comparison of EAM and central-force potentials, in: V. Vitek, D.J. Srolovitz (Eds.), Atomistic Simulation of Materials, Springer, Boston, 1989, pp. 245–263.
[2] T. Watanabe, Grain boundary engineering: historical perspective and future prospects, J. Mater. Sci. 46 (2011) 4095–4115, https://doi.org/10.1007/s10853-011-5393-z.
[3] I.P. Semenova, R.Z. Valiev, E.B. Yakushina, G.H. Salimgareeva, T.C. Lowe, Strength and fatigue properties enhancement in ultrafine-grained Ti produced by severe

plastic deformation, J. Mater. Sci. 4 (2008) 7354–7359, https://doi.org/10.1007/s10853-008-2984-4.

[4] N. Vandewalle, G. Lumay, O. Gerasimov, F. Ludewig, Influence of grain shape, friction and cohesion on granular compaction dynamics, Eur. Phys. J. E. 22 (2007) 241–248, https://doi.org/10.1140/epje/e2007-00031-0.

[5] H.K. Lee, H. Baier, J.S. Park, Y.P. Lee, Y.S. Lee, Grain-size effects and the physical properties of La$_{0.7}$Ca$_{0.3}$MnO$_{3-\delta}$, Key Eng. Mater. 277–279 (2005) 929–934. https://doi.org/10.4028/www.scientific.net/kem.277-279.929.

[6] M. Becton, X. Wang, Grain-size dependence of mechanical properties in polycrystalline boron-nitride: a computational study, Phys. Chem. Chem. Phys. 17 (2015) 21894–21901, https://doi.org/10.1039/C5CP03460D.

[7] A. Isacsson, A.W. Cummings, L. Colombo, J.M. Kinaret, S. Roche, Scaling properties of polycrystalline graphene: a review, 2D Mater. 4 (2017), https://doi.org/10.1088/2053-1583/aa5147, 012002 -1-12.

[8] M.A. Meyers, A. Mishra, D.J. Benson, Mechanical properties of nanocrystalline materials, Prog. Mater. Sci. 51 (2006) 427–556, https://doi.org/10.1016/j.pmatsci.2005.08.003.

[9] A.J. Minnich, M.S. Dresselhaus, Z.F. Ren, G. Chen, Bulk nanostructured thermoelectric materials: current research and future prospects, Energy Environ. Sci. 2 (2009) 466–479, https://doi.org/10.1039/b822664b.

[10] M.G. Kanatzidis, Nanostructured thermoelectrics: the new paradigm, Chem. Mater. 22 (2009) 648–659, https://doi.org/10.1021/cm902195j.

[11] Z.G. Chen, G. Han, L. Yang, L. Cheng, J. Zou, Nanostructured thermoelectric materials: current research and future challenge, Prog. Nat. Sci. Mater. Int. 22 (2012) 535–549, https://doi.org/10.1016/j.pnsc.2012.11.011.

[12] C.J. Vineis, A. Shakouri, A. Majumdar, M.G. Kanatzidis, Nanostructured thermoelectrics: big efficiency gains from small features, Adv. Mater. 22 (2010) 3970–3980, https://doi.org/10.1002/adma.201000839.

[13] K. Kishimoto, Y. Nagamoto, T. Miki, T. Koyanagi, Microstructure and thermoelectric properties of Cr-doped β-FeSi$_2$ sintered with micrograins treated in radio frequency plasmas of SiH$_4$ and GeH$_4$ gases, J. Appl. Phys. 92 (2002) 4393–4401, https://doi.org/10.1063/1.1507814.

[14] C.H. Kuo, H.S. Chien, C.S. Hwang, Y.W. Chou, M.S. Jeng, M. Yoshimura, Thermoelectric properties of fine-grained PbTe bulk materials fabricated by cryomilling and spark plasma sintering, Mater. Trans. 52 (2011) 795–801, https://doi.org/10.2320/matertrans.M2010331.

[15] S.V. Novikov, A.T. Burkov, X. Tang, Y. Yan, Thermoelectric properties of melt-spun and crystalline In$_{0.2}$Ce$_{0.1}$Co$_4$Sb$_{12.3}$ ribbons, Mater. Today. Proc. 8 (2019) 713–717, https://doi.org/10.1016/j.matpr.2019.02.072.

[16] G.J. Snyder, Figure of merit ZT of a thermoelectric device defined from materials properties, Energy Environ. Sci. 10 (2017) 2280–2283, https://doi.org/10.1039/c7ee02007d.

[17] O. Ivanov, O. Maradudina, R. Lyubushkin, Grain size effect on electrical resistivity of bulk nanograined Bi$_2$Te$_3$ material, Mater. Char. 99 (2015) 175–179, https://doi.org/10.1016/j.matchar.2014.12.001, 1044-5803.

[18] W. Kim, Strategies for engineering phonon transport in thermoelectrics, J. Mater. Chem. C. 3 (2015), https://doi.org/10.1039/C5TC01670C, 0336-10348.

[19] D. Choi, The electron scattering at grain boundaries in tungsten films, Microelectron. Eng. 122 (2014) 5–8, https://doi.org/10.1016/j.mee.2014.03.012.

[20] H. Wu, J. Carrete, Z. Zhang, Y. Qu, X. Shen, Z. Wang, L.D. Zhao, J. He, Strong enhancement of phonon scattering through nanoscale grains in lead sulfide thermoelectrics, NPG Asia Mater. 6 (2014) 2–11, https://doi.org/10.1038/am.2014.39, 2014.

[21] J.H. Bahk, Z. Bian, A. Shakouri, Electron transport modeling and energy filtering for efficient thermoelectric Mg$_2$Si$_{1-x}$Sn$_x$ solid solutions, Phys. Rev. B 89 (2014) 1–13, https://doi.org/10.1103/PhysRevB.89.075204, 075204.

[22] J.H. Bahk, Z. Bian, A. Shakouri, Electron energy filtering by a nonplanar potential to enhance the thermoelectric power factor in bulk materials, Phys. Rev. B 87 (2013) 1–13, https://doi.org/10.1103/PhysRevB.87.075204, 075204.

[23] Y. Xia, J. Park, F. Zhou, V. Ozolin, High thermoelectric power factor in intermetallic CoSi arising from energy filtering of electrons by phonon scattering, Phys. Rev. Appl. 11 (2019), https://doi.org/10.1103/PhysRevApplied.11.024017, 024017-1-8.

[24] Y. Pan, T.R. Wei, C.F. Wu, J.F. Li, Electrical and thermal transport properties of spark plasma sintered n-type Bi$_2$Te$_{3-x}$Se$_x$ alloys: the combined effect of point defect and Se content, J. Mater. Chem. C. 3 (2015) 10583–10589, https://doi.org/10.1039/C5TC02219C.

[25] L. Hu, T. Zhu, X. Liu, X. Zhao, Point defect engineering of high-performance bismuth-telluride-based thermoelectric materials, Adv. Funct. Mater. 24 (2014) 5211–5218, https://doi.org/10.1002/adfm.201400474.

[26] J. Suh, K.M. Yu, D. Fu, X. Liu, F. Yang, J. Fan, D.J. Smith, Y.H. Zhang, J.K. Furdyna, C. Dames, W. Walukiewicz, J. Wu, Simultaneous enhancement of electrical conductivity and thermopower of Bi$_2$Te$_3$ by multifunctionality of native defects, Adv. Mater. 27 (2015) 3681–3686, https://doi.org/10.1002/adma.201501350.

[27] S.D. Bhame, D. Pravarthana, W. Prellier, J.G. Noudem, Enhanced thermoelectric performance in spark plasma textured bulk n-type Bi$_2$Te$_{2.7}$Se$_{0.3}$ and p-type Bi$_{0.5}$Sb$_{1.5}$Te$_3$, Appl. Phys. Lett. 102 (2013), https://doi.org/10.1063/1.4807771, 2190-2191-3.

[28] X.A. Fan, J.Y. Yang, R.G. Chen, H.S. Yun, W. Zhu, S.Q. Bao, X.K. Duan, Characterization and thermoelectric properties of p-type 25%Bi$_2$Te$_3$–75%Sb$_2$Te$_3$ prepared via mechanical alloying and plasma activated sintering, J. Phys. D Appl. Phys. 39 (2006) 740–745, https://doi.org/10.1088/0022-3727/39/4/021.

[29] J. Jiang, L. Chen, S. Bai, Q. Yao, Q. Wang, Fabrication and thermoelectric performance of textured n-type Bi$_2$(Te,Se)$_3$ by spark plasma sintering, Mater. Sci. Eng. B. 117 (2005) 334–338, https://doi.org/10.1016/j.mseb.2005.01.002.

[30] Q. Lognon, F. Gascoin, O.I. Lebedev, L. Lutterotti, S. Gascoin, D. Chateigner, Quantitative texture analysis of spark plasma textured n-Bi$_2$Te$_3$, J. Am. Ceram. Soc. 97 (2014) 2038–2045, https://doi.org/10.1111/jace.12970.

[31] A. Vasil'ev, M. Yaprintsev, O. Ivanov, E. Danshina, Anisotropic thermoelectric properties of Bi$_{1.9}$Lu$_{0.1}$Te$_{2.7}$Se$_{0.3}$ textured via spark plasma sintering, Solid State Sci. 84 (2018) 28–43, https://doi.org/10.1016/j.solidstatesciences.2018.08.004.

[32] Y. Morisaki, H. Araki, H. Kitagawa, M. Orihashi, K. Hasezaki, K. Kimura, Bi$_2$Te$_3$-related thermoelectric samples with aligned-texture prepared by plastic deformation, Mater. Trans. 46 (2005) 2518–2524, https://doi.org/10.2320/matertrans.46.2518.

[33] M. Yaprintsev, A. Vasil'ev, O. Ivanov, Thermoelectric properties of the textured Bi$_{1.9}$Gd$_{0.1}$Te$_3$ compounds spark-plasma-sintered at various temperatures, J. Eur. Ceram. Soc. 40 (2020) 742–750, https://doi.org/10.1016/j.jeurceramsoc.2018.12.041.

[34] O. Ben-Yehuda, R. Shuker, Y. Gelbstein, Z. Dashevsky, M.P. Dariel, Highly textured Bi$_2$Te$_3$-based materials for thermoelectric energy conversion, J. Appl. Phys. 101 (2007), https://doi.org/10.1063/1.2743816, 113707-1-6.

[35] J.J. Shen, L.P. Hu, T.J. Zhu, X.B. Zhao, The texture related anisotropy of thermoelectric properties in bismuth telluride based polycrystalline alloys, Appl. Phys. Lett. 99 (2011), https://doi.org/10.1063/1.3643051, 124102-1-3.

[36] X. Yan, B. Poudel, W.S. Liu, G. Joshi, H. Wang, Y. Lan, D. Wang, G. Chen, Z.F. Ren, Experimental studied on anisotropic thermoelectric properties and structures of n-type Bi$_2$Te$_{2.7}$Se$_{0.3}$, Nano Lett. 10 (2010) 3373–3378, https://doi.org/10.1021/nl101156v.

[37] E. Symeou, Ch Nicolaou, A. Delimitis, J. Androulakis, Th Kyratsi, J. Giapintzakis, High thermoelectric performance of Bi$_{2-x}$Sb$_x$Te$_3$ bulk alloys prepared from non-nanostructured starting powders, J. Solid State Chem. 270 (2019) 388–397, https://doi.org/10.1016/j.jssc.2018.11.037.

[38] R. Deng, X. Su, Z. Zheng, W. Liu, Y. Yan, Q. Zhang, V.P. Dravid, C. Uher, M.G. Kanatzidis, X. Tang, Thermal conductivity in Bi$_{0.5}$Sb$_{1.5}$Te$_{3+x}$ and the role of dense dislocation arrays at grain boundaries, Sci. Adv. 4 (2018), https://doi.org/10.1126/sciadv.aar5606 eaar5606.

[39] Y. Li, F. Li, J. Dong, Z.H. Ge, F. Kang, J. He, H. Du, B. Li, J. Li, Enhanced mid-temperature thermoelectric performance of textured SnSe polycrystals made of solvothermally synthesized powders, J. Mater. Chem. C. 4 (2016) 2047–2055, https://doi.org/10.1039/C5TC04202J.

[40] D. Feng, Z.H. Ge, D. Wu, Y.X. Chen, T. Wu, J. Li, J. He, Enhanced thermoelectric properties of SnSe polycrystals via texture control, Phys. Chem. Chem. Phys. 18 (2016) 31821–31827, https://doi.org/10.1039/c6cp06466c.

[41] S.R. Popuri, M. Pollet, R. Decourt, F.D. Morrison, N.S. Bennett, J.W.G. Bos, Large thermoelectric power factors and impact of texturing on the thermal conductivity in polycrystalline SnSe, J. Mater. Chem. C. 4 (2016) 1685–1691, https://doi.org/10.1039/C6TC00204H.

[42] A. Novitskii, G. Guelou, D. Moskovskikh, A. Voronin, E. Zakharova, L. Shvanskaya, A. Bogach, A. Vasilev, V. Khovaylo, T. Mori, Reactive spark plasma sintering and thermoelectric properties of Nd-substituted BiCuSeO oxyselenides, J. Alloys Compd. 785 (2019) 96–104, https://doi.org/10.1016/j.jallcom.2019.01.183.

[43] M.-E. Song, H. Lee, M.-G. Kang, W. Li, D. Maurya, B. Poudel, J. Wang, M.A. Meeker, G.A. Khodaparast, S.T. Huxtable, S. Priya, Nanoscale texturing and interfaces in compositionally modified Ca$_3$Co$_4$O$_9$ with enhanced thermoelectric performance, ACS Omega 3 (2018) 10798–10810, https://doi.org/10.1021/acsomega.8b01552.

[44] W. Li, J. Wang, B. Poudel, H.B. Kang, S. Huxtable, A. Nozariasbmarz, U. Saparamadu, S. Priya, Filiform metal silver nanoinclusions to enhance thermoelectric performance of p-type Ca$_3$Co$_4$O$_{9+\delta}$ oxide, ACS Appl. Mater. Interfaces 11 (2019) 42131–42138, https://doi.org/10.1021/acsami.9b13607.

[45] M. Yaprintsev, A. Vasil'ev, O. Ivanov, Sintering temperature effect on thermoelectric properties and microstructure of the grained Bi$_{1.9}$Gd$_{0.1}$Te$_3$ compound, J. Eur. Ceram. Soc. 39 (2019) 1193–1205, https://doi.org/10.1016/j.jeurceramsoc.2018.12.041.

[46] J. Yang, F. Wu, Z. Zhu, L. Yao, H. Song, X. Hu, Thermoelectrical properties of lutetium-doped Bi$_2$Te$_3$ bulk samples prepared from flower-like nanopowders, J. Alloys Compd. 619 (2015) 401–405, https://doi.org/10.1016/j.jallcom.2014.09.024.

[47] X.H. Ji, X.B. Zhao, Y.H. Zhang, B.H. Lu, H. Ni, Synthesis and properties of rare earth containing Bi$_2$Te$_3$ based thermoelectric alloys, J. Alloys Compd. 387 (2005) 282–286, https://doi.org/10.1016/j.jallcom.2004.06.047.

[48] F. Wu, H. Song, J. Jia, X. Hu, Effects of Ce, Y, and Sm doping on the thermoelectric properties of Bi$_2$Te$_3$ alloy, Prog. Nat. Sci. Mater. Int. 23 (2013) 408–412, https://doi.org/10.1016/j.pnsc.2013.06.007.

[49] F. Wu, W. Shi, X. Hu, Preparation and thermoelectric properties of flower-like nanoparticles of Ce-Doped Bi$_2$Te$_3$, Electron, Mater. Lett. 11 (2015) 127–132, https://doi.org/10.1007/s13391-014-4139-x.

[50] X.H. Ji, X.B. Zhao, Y.H. Zhang, B.H. Lu, H.L. Ni, Solvothermal synthesis and thermoelectric properties of lanthanum contained Bi–Te and Bi–Se–Te alloys, Mater. Lett. 59 (2005) 682–685, https://doi.org/10.1016/j.matlet.2004.11.008.

[51] F. Wu, H.Z. Song, J.F. Jia, F. Gao, Y.J. Zhang, X. Hu, Thermoelectric properties of Ce-doped n-type Ce$_x$Bi$_{2-x}$Te$_{2.7}$Se$_{0.3}$ nanocomposites, Phys. Status Solidi 210 (2013) 1183–1189, https://doi.org/10.1002/pssa.201228589.

[52] W.Y. Shi, F. Wu, K.L. Wang, J.J. Yang, H.Z. Song, X.J. Hu, Preparation and thermoelectric properties of yttrium-doped Bi$_2$Te$_3$ flower-like nanopowders, J. Electron. Mater. 43 (2014) 3162–3168, https://doi.org/10.1007/s11664-014-3220-4.

[53] X.B. Zhao, Y.H. Zhang, X.H. Ji, Solvothermal synthesis of nano-sized La$_x$Bi$_{(2-x)}$Te$_3$ thermoelectric powders, Inorg. Chem. Commun. 7 (2004) 386–388, https://doi.org/10.1016/j.inoche.2003.12.020.

[54] O. Ivanov, M. Yaprintsev, R. Lyubushkin, O. Soklakova, Enhancement of thermoelectric efficiency in Bi_2Te_3 via rare earth element doping, Scripta Mater. 146 (2018) 91–94, https://doi.org/10.1016/j.scriptamat.2017.11.031.

[55] M. Yaprintsev, R. Lyubushkin, O. Soklakova, O. Ivanov, Effects of Lu and Tm doping on thermoelectric properties of Bi_2Te_3, J. Electron. Mater. 47 (2018) 1362–1370, https://doi.org/10.1007/s11664-017-5940-8.

[56] O. Ivanov, M. Yaprintsev, Mechanisms of thermoelectric efficiency enhancement in Lu-doped Bi_2Te_3, Mater. Res. Express 5 (2018), https://doi.org/10.1088/2053-1591/aaa265, 015905-1-10.

[57] H.J. Goldsmid, Bismuth telluride and its alloys as materials for thermoelectric generation, Mater 7 (2014) 2577–2592, https://doi.org/10.3390/ma7042577.

[58] H. Scherrer, S. Scherrer, Thermoelectrics Handbook: Macro to Nano, CRC Taylor and Francis, Boca Raton, 2012.

[59] G.S. Nolas, J. Sharp, H.J. Goldsmid, Thermoelectrics Basic Principles and New Materials Developments, Springer, Berlin, 2001.

[60] F.K. Lotgering, Topotactical reactions with ferrimagnetic oxides having hexagonal crystal structures—I, J. Inorg. Nucl. Chem. 9 (1959) 113–123, https://doi.org/10.1016/0022-1902(59)80070-1.

[61] Z.A. Munir, U. Anselmi-Tamburini, M. Ohyanagi, The effect of electric field and pressure on the synthesis and consolidation of materials: a review of the spark plasma sintering method, J. Mater. Sci. 41 (2006) 763–777, https://doi.org/10.1007/s10853-006-6555-2.

[62] Z.A. Munir, D.V. Quach, M. Ohyanagi, Electric current activation of sintering: a review of the pulsed electric current sintering process, J. Am. Ceram. Soc. 94 (2011) 1–19, https://doi.org/10.1111/j.1551-2916.2010.04210.x.

[63] Y. Sun, K. Kulkarni, A.K. Sachdev, E.J. Lavernia, Synthesis of γ-TiAl by reactive spark plasma sintering of cryomilled Ti and Al powder blend: Part II: effects of electric field and microstructure on sintering kinetics, Metall. Mater. Trans. 45 (2014) 2759–2767, https://doi.org/10.1007/s11661-014-2216-2.

[64] D. Jiang, D.M. Hulbert, J.D. Kuntz, U. Anselmi-Tamburini, A.K. Mukherjee, Spark plasma sintering: a high strain rate low-temperature forming tool for ceramics, Mater. Sci. Eng. 463 (2007) 89–93, https://doi.org/10.1016/j.msea.2006.07.163.

[65] O. Ivanov, O. Soklakova, R. Lyubushkin, A. Voronin, Grain structure evolution at sintering of the bulk Bi_2Te_3 nanomaterial under hot pseudo-isostatic pressure, J. Mater. Sci. 51 (2016) 3415–3421, https://doi.org/10.1007/s10853-015-9658-9.

[66] M.J. Aziz, Pressure and stress effects on diffusion in Si, Defect Diffusion Forum 153–155 (1998) 1–10. https://doi.org/10.4028/www.scientific.net/DDF.153-155.1.

[67] H. Park, K.S. Jones, J.A. Slinkman, M.E. Law, Effect on hydrostatic pressure on dopant diffusion in silicon, J. Appl. Phys. 78 (1995) 3664–3670, https://doi.org/10.1063/1.359944.

[68] F.J. Humphreys, M. Hatherly, Recrystallization and Related Annealing Phenomena, Elsevier, Oxford, UK, 2004.

[69] J. Burke, D. Turnbull, Recrystallization and grain growth, Prog. Met. Phys. 3 (1952) 220–292, https://doi.org/10.1016/0502-8205(52)90009-9.

[70] J.K.L. Lai, C.H. Shek, G.M. Lin, Grain growth kinetics of nanocrystalline SnO_2 for long-term isothermal annealing, Scripta Mater. 49 (2003) 441–446, https://doi.org/10.1016/S1359-6462(03)00296-3.

[71] B. Sapoval, C. Hermann, Physics of Semiconductors, Springer-Verlag, New York, 1995.

[72] J.S. Blakemore, Solid State Physics, Cambridge University Press, Cambridge, UK, 1985.

[73] S. Wang, J. Yang, T. Toll, J. Yang, W. Zhang, X. Tang, Conductivity-limiting bipolar thermal conductivity in semiconductors, Sci. Rep. 5 (2015), https://doi.org/10.1038/srep10136, 10136-1-5.